Research Square

Preprints are preliminary reports that have not undergone peer review.
They should not be considered conclusive, used to inform clinical practice,
or referenced by the media as validated information.

# Hydrogen Sensing Properties of Functionalized Graphite–Palladium Nanocomposites: Correlated Structural, Spectroscopic and Charge-Transfer Driven detection Mechanism

**Papiya Saha**
Sathyabama Institute of Science and Technology
**Binaya Kumar Sahu**
binayamsc12@gmail.com
Panchayat College Bargarh
**Shubham Roy**
Harbin Institute of Technology
**Rabindra Nath Juine**
Bhabha Atomic Research Centre

**Research Article**

**Keywords:** Hydrogen sensor, Palladium nanoparticles, functionalised graphite, Chemiresistor, Raman spectroscopy, Interdigitated electrode

**Posted Date:** August 20th, 2026

**DOI:** https://doi.org/10.21203/rs.3.rs-10420621/v1

**License:** This work is licensed under a Creative Commons Attribution 4.0 International License.
Read Full License

**Additional Declarations:** No competing interests reported.

# Hydrogen Sensing Properties of Functionalized Graphite–Palladium Nanocomposites: Correlated Structural, Spectroscopic and Charge-Transfer Driven detection Mechanism

Papiya Saha[1,*], Binaya Kumar Sahu[2,*], Shubham Roy[3,*], Rabindra Nath Juine[4]

[1]*Department of Physics, Sathyabama Institute of Science and Technology, Chennai 600119, India.*

[2]*Department of Physics, Panchayat Degree College, Sambalpur University, Odisha 768028, India.*

[3]*School of Science, Harbin Institute of Technology, Shenzhen, China.*

[4]*Health Physics Division, Bhabha Atomic Research Centre, Mumbai 400085, India.*

*Corresponding authors: papiya.saha.physics@sathyabama.ac.in (P.S), binayamsc12@gmail.com (BKS), shubham.royju@gmail.com (SR)

## Abstract

Functionalised graphite–palladium (Pd/f-graphite) nanocomposites were synthesised via a wet-chemical route and evaluated as low-cost, room-temperature chemiresistive hydrogen sensors. Bulk graphite flakes were oxidatively treated in a 3:1 $H_2SO_4$ and $HnO_3$ mixture to generate edge and basal-plane defects bearing –COOH, –OH, and C=O groups. This functional group serve as anchoring sites for Pd nanoparticles. Palladium was incorporated at 20 and 33 wt% through $PdCl_2$ reduction using NaOH/$NaBH_4$. FESEM and TEM reveal well-dispersed Pd nanoparticles (8–12 nm), with denser and more uniform coverage at 33 wt%. XRD verifies face-centred-cubic Pd with an average crystallite size of ~9 nm (Scherrer), consistent with TEM, on a well-ordered graphitic lattice. FT-IR elucidates oxygen functionalities and their partial consumption upon Pd coordination. Raman spectroscopy establishes the multilayer/bulk nature of graphite (I(2D)/I(G) < 1 with a broadened, up-shifted 2D band. In addition, peak originated at 440 and 650 $cm^{-1}$ correspond to $E_g$ and $B_{1g}$ modes of PdO, indicating partial surface oxidation of the metal. Finally, Devices were fabricated by drop-casting samples with varied concentration of Pd loaded on f-graphite onto interdigitated (IDE) and two-fringe electrodes exhibit reversible resistance increases upon $H_2$ exposure. The 33 wt% Pd/f-graphite IDE device shows optimal performance, achieving 21.3% sensitivity toward 4 vol% $H_2$ in air at 25 °C, decreasing monotonically to 1 vol%. The sensing response is proposed to arise from a PdHx-mediated work-function modulation and charge-transfer mechanism in weakly p-type graphite, with $O_2$-assisted recovery. Raman-derived defect evolution and G-band softening (1592→1576 $cm^{-1}$) provide direct evidence of Pd→graphite electron transfer, supported by Langmuir/first-order kinetics, establishing an interface-controlled sensing mechanism.

**Keywords:** Hydrogen sensor; Palladium nanoparticles; functionalised graphite; Chemiresistor; Raman spectroscopy; Interdigitated electrode.

## 1. Introduction

The shift to a low-carbon energy economy has boosts an interest in hydrogen as a clean energy source thanks to its controlled combustion process which produces energy with only water as a byproduct [1, 2]. Oweing to its greter diffusion co-efficient than that of petrol or natural gas, hydrogen is a wiser alternative in fuel cells, transportation, aerospace propulsion, and many industrial operations [3-6]. However, hydrogen has a lower flammability limit of around 4 vol% in air; concentrations over this threshold can burn and burst [4, 7, 8]. In addition, hydrogen is colourless, odourless, and highly explosive [9]. For distributed safety monitoring, chemiresistive sensors that function at ambient temperature with low power, low cost, and straightforward readout electronics are especially appealing [10-12]. Therefore, reliable detection of hydrogen leakage well below the prescribed limit is highly required.

In that direction, palladium (Pd) is the established as a hydrogen sensing metal thanks to its high hydrogen solubility and diffusivity [13]. Hence, $H_2$ dissociates readily on Pd surface and is absorbed to form a palladium hydride ($PdH_x$) phase whose electronic properties differ markedly from those of the pristine metal [14, 15]. However, bare Pd nanoparticles agglomerate and lose active surface area with time, whereas continuous Pd films are costly and often split and delaminate following repeated α↔β hydride cycling [16]. Both issues can be mitigated by introducing a charge-transduction channel by dispersing Pd on a conductive, chemically stable substrate. As a result, Pd-decorated carbon nanomaterials such as carbon nanotubes, graphene, and reduced graphene oxide emerged as a leading platform for room-temperature hydrogen sensing [17-26].

Unlike graphene, bulk graphite is inexpensive, abundant, highly conductive, and the most stable carbon allotrope under ambient conditions. Its layered $sp^2$ structure, however, is chemically inert and offers few anchoring sites for metal nucleation. Aggressive oxidative treatment with $H_2SO_4/HNO_3$ introduces defects and oxygen functional groups (–COOH, –OH, C=O) at the edges and, to a lesser extent, the basal planes of the graphite crystallites; these sites both improve aqueous dispersibility and template the growth of Pd nanoparticles [27-30].

In this work, we synthesised functionalised graphite (f-graphite) as a cost-effective Pd support and created chemiresistive sensors by simple drop-casting onto two electrode geometries (interdigitated and two-fringe). We further investigate FESEM, TEM, XRD and FT-IR, to validate the integration of metal nanoparticles in the graphite. Importantly, Raman spectroscopy is used to corroborate the optimised interfacial engineering for sensing. The effects of Pd loading (20 vs 33 wt%), hydrogen concentration (1–4 vol%), and electrode geometry on sensitivity, response, and recovery are examined and mechanistically deciphered.

## 2. Experimental

### 2.1. Functionalisation of graphite

A typical acid treatment was used to functionalise graphite flakes. The flakes were obtained from Bay Carbon, USA and distributed in a 3:1 solution of concentrated $H_2SO_4$ and $HNO_3$, ultrasonicated for about 15 minutes, and then continuously stirred at room temperature for 16 hours. The suspension was vacuum-filtered, washed repeatedly with de-ionised water, and dried overnight at 60 °C in a vacuum oven. This treatment is supposed to decrease the crystallite size of graphite, along with the introduction of structural defects and oxygen functional groups (–COOH, –OH, C=O), preferentially at graphite edges and partially on the basal surface. The as-prepared sample is denoted as f-graphite.

### 2.2. Synthesis of Pd/f-graphite nanocomposites

For the synthesis of the composite, f-graphite was first dispersed in de-ionised water by ultrasonication (≈15 min) and stirred continuously. $PdCl_2 \cdot 2H_2O$ obtained from SRL Chemicals, India, was used as the Pd precursor. A calculated volume of 1 wt% aqueous $PdCl_2$ was added drop-wise to the flake solution and the mixture was stirred for 24 h. This process allows $Pd^{2+}$ ions to coordinate to the oxygen functional groups of f- graphite by ion exchange. Further, 1 M NaOH and 0.1 M $NaBH_4$ were then added dropwise, and stirring was continued for a further 24 h to reduce the bound $Pd^{2+}$ to metallic Pd nanoparticles. The final product was vacuum-filtered, washed several times with de-ionised water and dried at 60 °C. Two Pd loadings, 20 and 33 wt%, were obtained by varying the amount of $PdCl_2$ solution added and were named Pd (20 wt%)/f-graphite and Pd (30 wt%)/f-graphite, respectively.

### 2.3. Characterisation

X-ray diffraction was recorded at room temperature on a Philips X'Pert Pro diffractometer (Cu Kα, λ = 0.1542 nm; 40 kV, 30 mA) over 2θ = 10–90° in steps of 0.016°. Crystallite and particle sizes from XRD were estimated with the Scherrer equation. FT-IR spectra (400–4000 $cm^{-1}$) were collected on a PerkinElmer spectrometer from KBr pellets. Raman spectra (100–3000 $cm^{-1}$) were acquired on a WITec alpha300 confocal Raman microscope using Nd:YAG laser excitation of 532 nm. Morphology was examined by FESEM (FEI Quanta) and TEM.

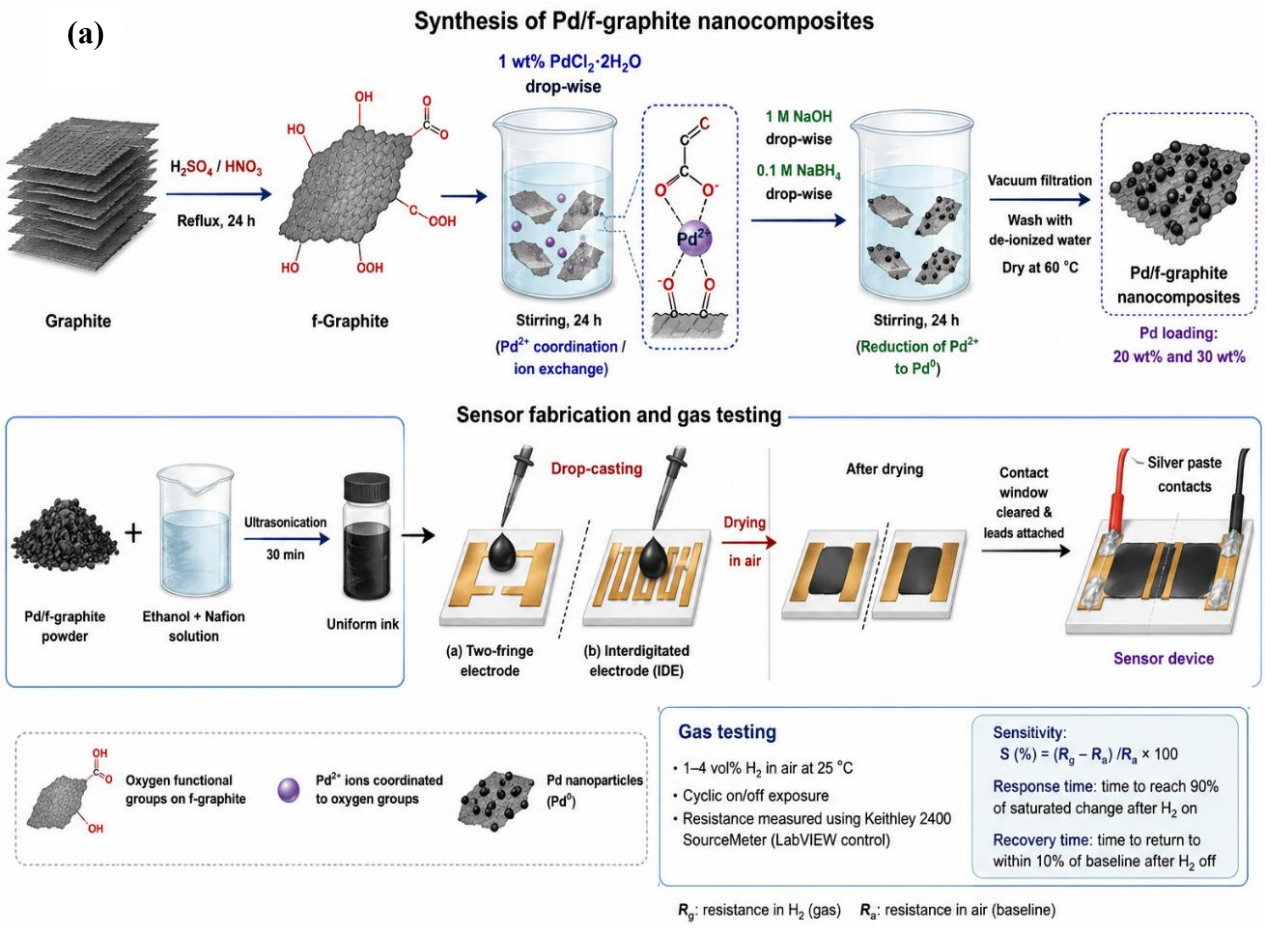
### 2.4. Sensor fabrication and gas testing

The powders were dispersed in ethanol:Nafion to form a uniform ink, which was then drop-cast onto alumina substrates patterned with copper electrodes of two geometries—a two-fringe type and an interdigitated electrode (IDE). After drying in air, the contact windows were cleaned and the

leads were attached with silver paste. Resistance was measured using a Keithley 2400 source meter and LabVIEW control while the films were exposed to 1–4 vol% $H_2$ in air at 25 °C in cyclic on/off sequences. The sensor response in terms of sensitivity is defined as:

$$S\ (\%) = (R_g - R_a) / R_a \times 100,$$

where $R_g$ and $R_a$ are the film resistances in the presence of gas (hydrogen) and in air. The response time is the time to reach 90% of the saturated change after $H_2$ admission and the recovery time is the time to return to within 10% of the baseline after $H_2$ removal. The detailed synthesis of the composite and the sensor fabrication are depicted in Figure 1.



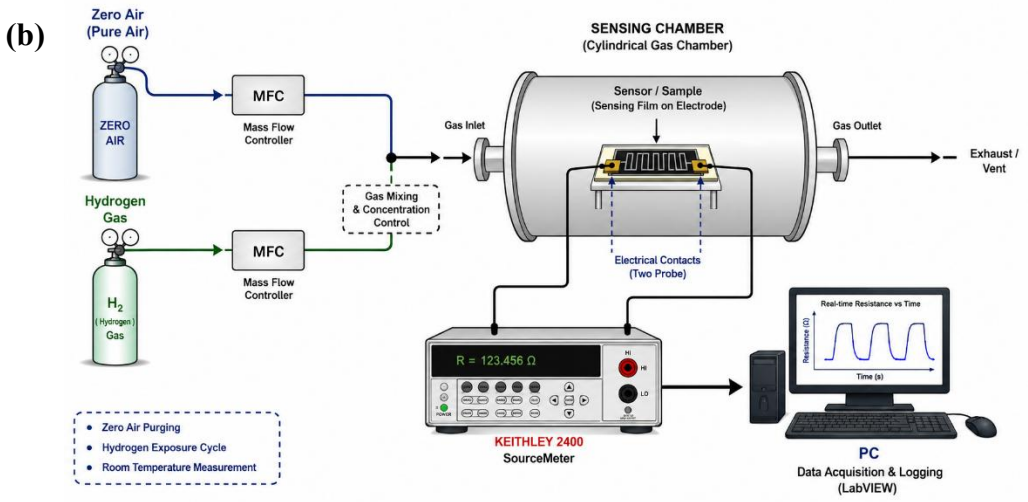



**Figure 1.** Schematic of the (a) sensor fabrication flow: acid functionalisation of graphite, coordination-assisted Pd decoration, ink formulation and drop-casting onto the electrode;(b) sensing chamber connected with Zero air and $H_2$ gas and IDE sensor with electrical read out

## 3. Results and Discussion

### 3.1. Morphology and microstructure

Functionalisation occurs mainly at the edges and defect sites of the graphite crystallites, generating the –COOH/–OH/C=O groups that disperse f-graphite in water and bind $Pd^{2+}$ ions; upon reduction, Pd nucleates and grows preferentially at these sites [27-30]. Field-emission scanning electron microscopy (FESEM) images (Figure 2) illustrate the distribution of Pd nanoparticles over the graphite flakes for both loadings. The 20 wt% Pd sample (Figure 2a) shows a relatively thin and somewhat heterogeneous distribution of nanoparticles across the graphite surface. In contrast, the 33 wt% Pd sample (Figure 2b) exhibits a denser and more uniform nanoparticle population. This trend is consistent with the higher Pd loading, which increases the number of occupied nucleation sites. Nevertheless, owing to the inherently non-uniform functionalisation of bulk graphite, some degree of localised clustering is observed in both samples.

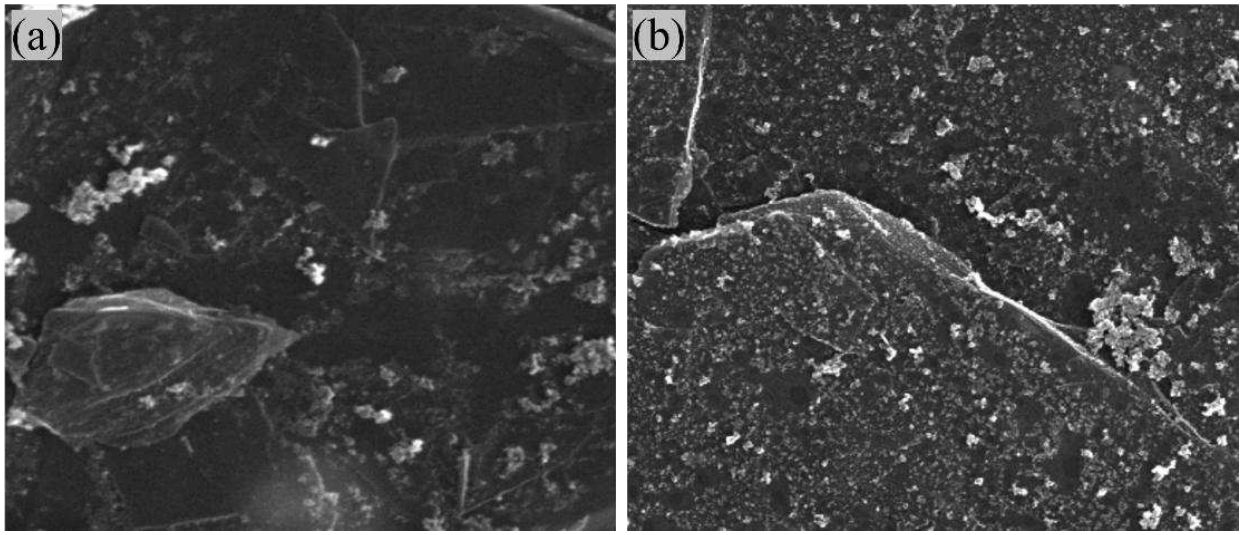



**Figure 2.** FESEM images of (a) Pd (20 wt%)/f-graphite and (b) Pd (33 wt%)/f-graphite, showing Pd nanoparticles dispersed on graphite flakes

Transmission electron microscopy (TEM) images (Figure 3) provide further insight into the morphology, revealing well-dispersed Pd nanoparticles with an average size of approximately 8–12 nm. Figure 3a shows the dispersed Pd on the graphite surface for Pd (20 wt%)/f-graphite and the inset shows the particle distribution (inset Figure 3a) with mean particle size 8 ± 1 nm. Similar distribution is observed Pd (33 wt%)/f-graphite with mean particle size 9 ± 1 nm (inset Figure 3a). Partial agglomeration into larger aggregates is evident after drying and conversion of the dispersion into powder, likely driven by capillary forces and interparticle interactions during solvent evaporation.

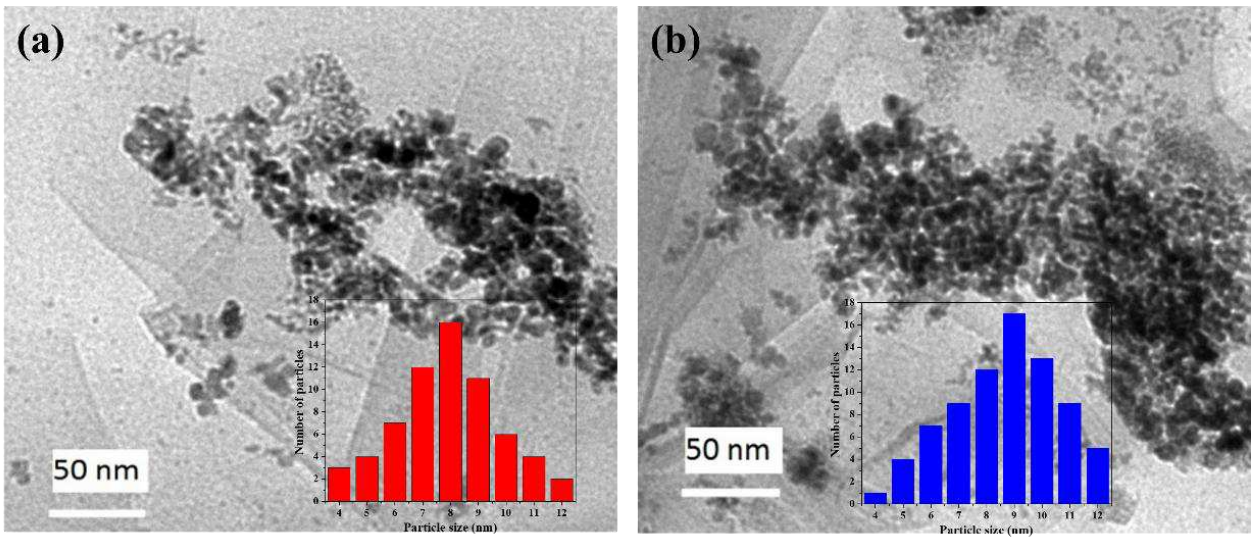



**Figure 3.** TEM images of (a) Pd (20 wt%)/f-graphite and (b) Pd (33 wt%)/f-graphite (inset) particle size distribution.

### 3.2. Phase and crystallite analysis (XRD)

Figure 4 shows the XRD patterns of graphite, f-graphite, Pd (20 wt%)/f-graphite and Pd (33 wt%)/f-graphite. All four patterns are dominated by the sharp graphite C(002) reflection at $2\theta \approx 26.6°$ (interlayer spacing ≈ 0.335 nm), together with the C(101) and C(004) reflections near 44.8° and 54.7°, confirming a well-ordered hexagonal graphitic lattice. The Pd-loaded composites (Figure 4c & d) display additional peaks and those are assigned to face-centred-cubic Pd: the Pd(111) peak near $2\theta \approx 40°$ and the weaker Pd(200) feature at higher angle. Applying the Scherrer equation to the broadened Pd(111) reflection gives an average Pd crystallite size of ≈9 nm, in excellent agreement with the 8–12 nm particle size measured by TEM as depicted in the previous section [31]. The Pd reflections are more intense for the 33 wt% sample, consistent with the higher metal content seen in FESEM.

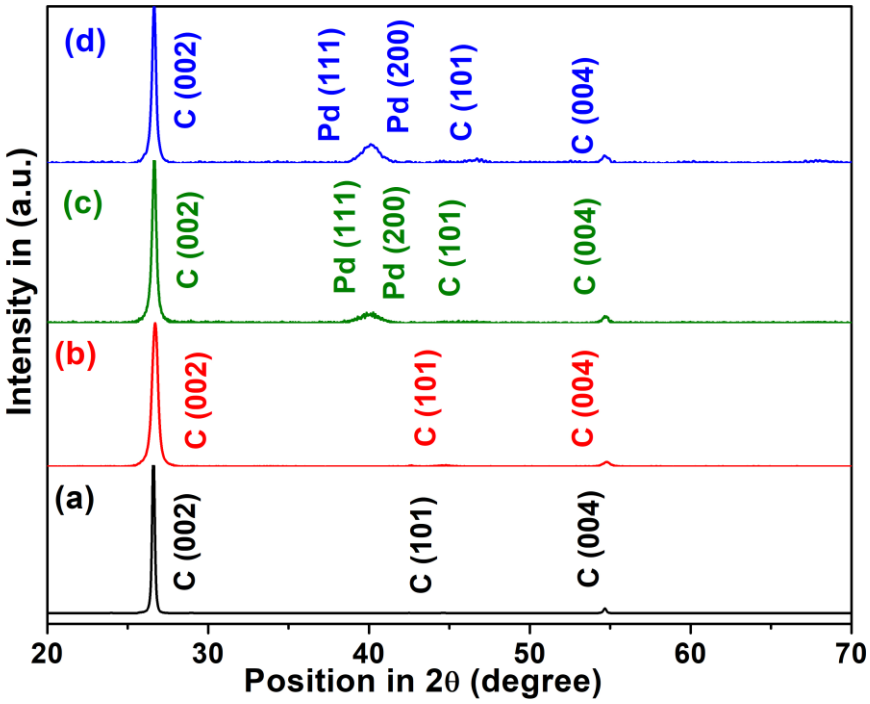



**Figure 4.** XRD patterns of (a) graphite, (b) f-graphite, (c) Pd (20 wt%)/f-graphite and (d) Pd (33 wt%)/f-graphite.

### 3.3. Surface functional groups (FT-IR)

FT-IR spectra confirm the oxidative functionalisation shown in Figure 5. Relative to pristine graphite, f-graphite develops bands near 1585, 1466, 1384 and 587 $cm^{-1}$ associated with C=O, carboxylate ($–COO^-$) and related oxygen functionalities. A broad band near 3470 $cm^{-1}$ occurs due to O–H stretching of –OH groups and adsorbed water. Further, bands at ≈2925 and 2850 $cm^{-1}$ can be

assigned to asymmetric and symmetric C–H stretching, and a band near 1048 $cm^{-1}$ from C–O/C–OH stretching, as shown in Figures 5a & b [30, 32]. After Pd loading (Figure 5c & d), several of these oxygen-related bands weaken, indicating that Pd coordinates to the oxygen functional groups during nucleation. The molecular-level counterpart of the site-selective decoration seen in FESEM and of the ion-exchange growth mechanism is clearly evident from FTIR spectra. Residual surface oxygen also makes the formation of a thin surface oxide (PdO) plausible, which is independently confirmed by Raman spectroscopy in the upcoming section.

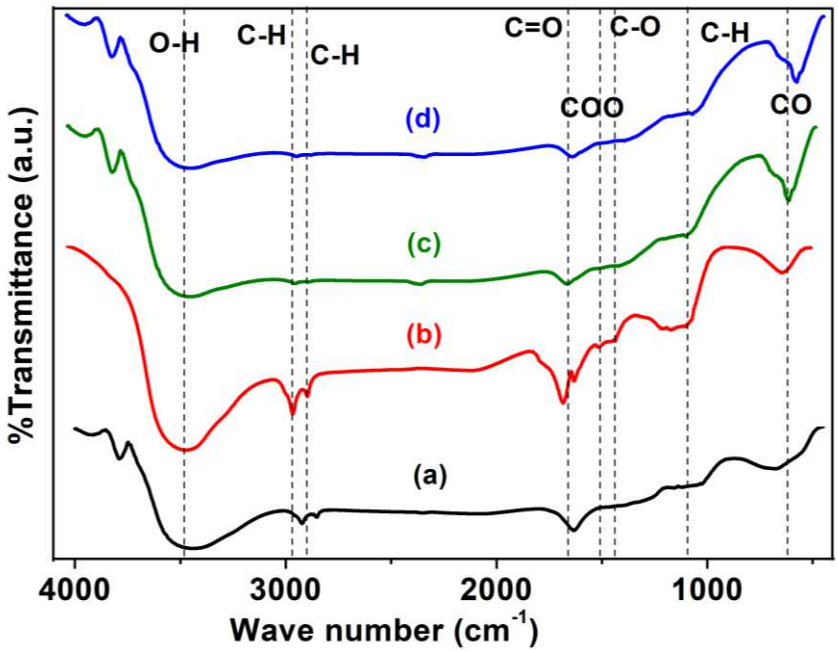



**Figure 5.** FT-IR spectra of (a) graphite, (b) f-graphite, (c) Pd (20 wt%)/f-graphite and (d) Pd (33 wt%)/f-graphite. Oxygen functionalities appear after functionalisation and are partly attenuated after Pd coordination.

### 3.4. Raman spectroscopy: graphite versus graphene, and identification of PdO

Raman spectroscopy (Figure 6) provides the nature of the carbon support and the Pd surface chemistry. Pristine graphite (Figure 6a) shows an intense G band near 1582 $cm^{-1}$ (in-plane $E_{2g}$ stretching of $sp^2$ carbon) and a broad 2D band near 2700–2720 $cm^{-1}$, with the defect-activated D band essentially absent—the signature of well-ordered, nearly defect-free graphite [33, 34]. After functionalisation (Figure 6b), a clear D band emerges at ≈1350 $cm^{-1}$, confirming that acid treatment generates the edge and basal-plane defects that act as Pd anchoring sites and that also broaden the XRD spectra as depicted in Figure 4b-d.

Crucially, the ratio I(2D)/I(G) is below unity in every spectrum (≈0.2–0.7) and the 2D band is broad, asymmetric and up-shifted relative to monolayer graphene. Single-layer graphene exhibits a sharp, symmetric 2D band near 2680 $cm^{-1}$ with I(2D)/I(G) ≈ 2–4, whereas multilayer or bulk graphite shows I(2D)/I(G) ≲ 0.5 with a broadened, up-shifted 2D band [35, 36]. The present spectra therefore establish unambiguously that the support is multilayer/bulk graphite, rather than graphene, consistent with the sharp, intense C(002) XRD reflection at 26.6° and with the bulk graphite-flake starting material (Figure 4a). This corrects the loose use of "graphene" that is common in the literature and fixes the correct electronic picture (a weakly p-type, semimetallic graphitic conductor) used in the sensing mechanism below.

The Pd-loaded samples (Figure 6c & d) show two additional low-frequency bands near 437/633 $cm^{-1}$ (20 wt%) and 428/642 $cm^{-1}$ (33 wt%). These are not generic "Pd nanoparticle" features—crystalline metallic Pd is Raman-inactive—but correspond to the Raman-active $E_g$ (≈440 $cm^{-1}$) and $B_{1g}$ (≈650 $cm^{-1}$) modes of PdO [37]. Their appearance only in the Pd-containing samples indicates a thin, partially oxidised PdO shell on the metallic Pd cores, in agreement with the residual surface oxygen seen by FT-IR. As discussed below, this surface oxide is mechanistically relevant to the oxygen-assisted recovery of the sensor.

In addition, the G-band position provides an independent, charge-transfer-sensitive probe. Relative to pristine graphite (1582 $cm^{-1}$), the G band of f-graphite up-shifts to 1592 $cm^{-1}$ ($\Delta \approx +10$ $cm^{-1}$), consistent with p-type doping introduced by the electron-withdrawing oxygen functional groups. Upon Pd loading, the G band shifts back down to 1584 $cm^{-1}$ (20 wt%) and 1576 $cm^{-1}$ (33 wt%, $\Delta \approx -6$ $cm^{-1}$ versus pristine graphite) indicating electron donation from Pd into the graphite lattice that softens the $E_{2g}$ phonon. Because the G-band frequency responds to both strain and doping, we attribute the monotonic loading-dependent softening primarily to charge transfer (doping) rather than strain: a strain-dominated shift would be expected to scale with particle-induced lattice distortion and to be mirrored by a comparable 2D-band shift, which is not observed, whereas the systematic G down-shift with increasing Pd content tracks the charge-transfer trend. This spectroscopic evidence for Pd→graphite electron transfer in the as-prepared state serves as the baseline on which the hydrogen-induced modulation in Section 3.5 operates, and it favours a charge-transfer-controlled rather than a purely geometric sensing model.

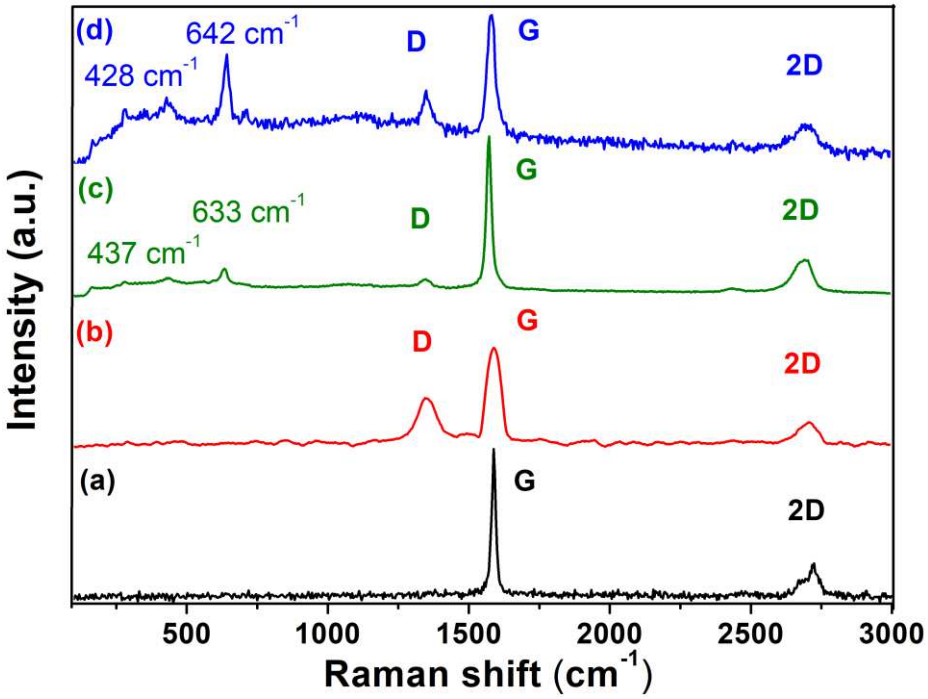



**Figure 6.** Raman spectra of (a) graphite, (b) f-graphite, (c) Pd (20 wt%)/f-graphite and (d) Pd (33 wt%)/f-graphite.

**Table 1.** Raman band positions and intensity ratios extracted from the spectra in Figure 6. The sub-unity I(2D)/I(G) values are diagnostic of bulk graphite. (PdO modes listed where present.)

| Sample | D ($cm^{-1}$) | G ($cm^{-1}$) | 2D ($cm^{-1}$) | I(D)/I(G) | I(2D)/I(G) |
|---|---|---|---|---|---|
| Graphite | absent | 1582 | ~2710 | 0.20 | 0.71 |
| f-graphite | 1351 | 1592 | ~2700 | 0.41 | 0.22 |
| Pd(20%)/f-graphite | 1351 | 1584 | ~2700 | 0.34 | 0.24 |
| Pd(33%)/f-graphite | 1351 | 1576 | ~2700 | 0.30 | 0.21 |

*PdO modes: Eg ≈ 437/428 $cm^{-1}$ and B1g ≈ 633/642 $cm^{-1}$ for the 20/33 wt% samples. Positions ±5 $cm^{-1}$.*

### 3.5. Hydrogen-sensing performance

Figure 7 shows the dynamic response of the four device configurations to successive pulses of 4, 3, 2 and 1 vol% $H_2$ in air at 25 °C. In every case, the sensitivity scales monotonically with hydrogen concentration, and the baseline is fully recovered between pulses. The 33 wt% Pd/f-graphite device on the interdigitated electrode (Figure 7a) is the most responsive, followed by the same composition on the two-fringe electrode (Figure 7b), then the 20 wt% devices (Figure 7c & d), exactly the ordering predicted by the dispersion and Pd-content trends from FESEM, TEM and XRD.

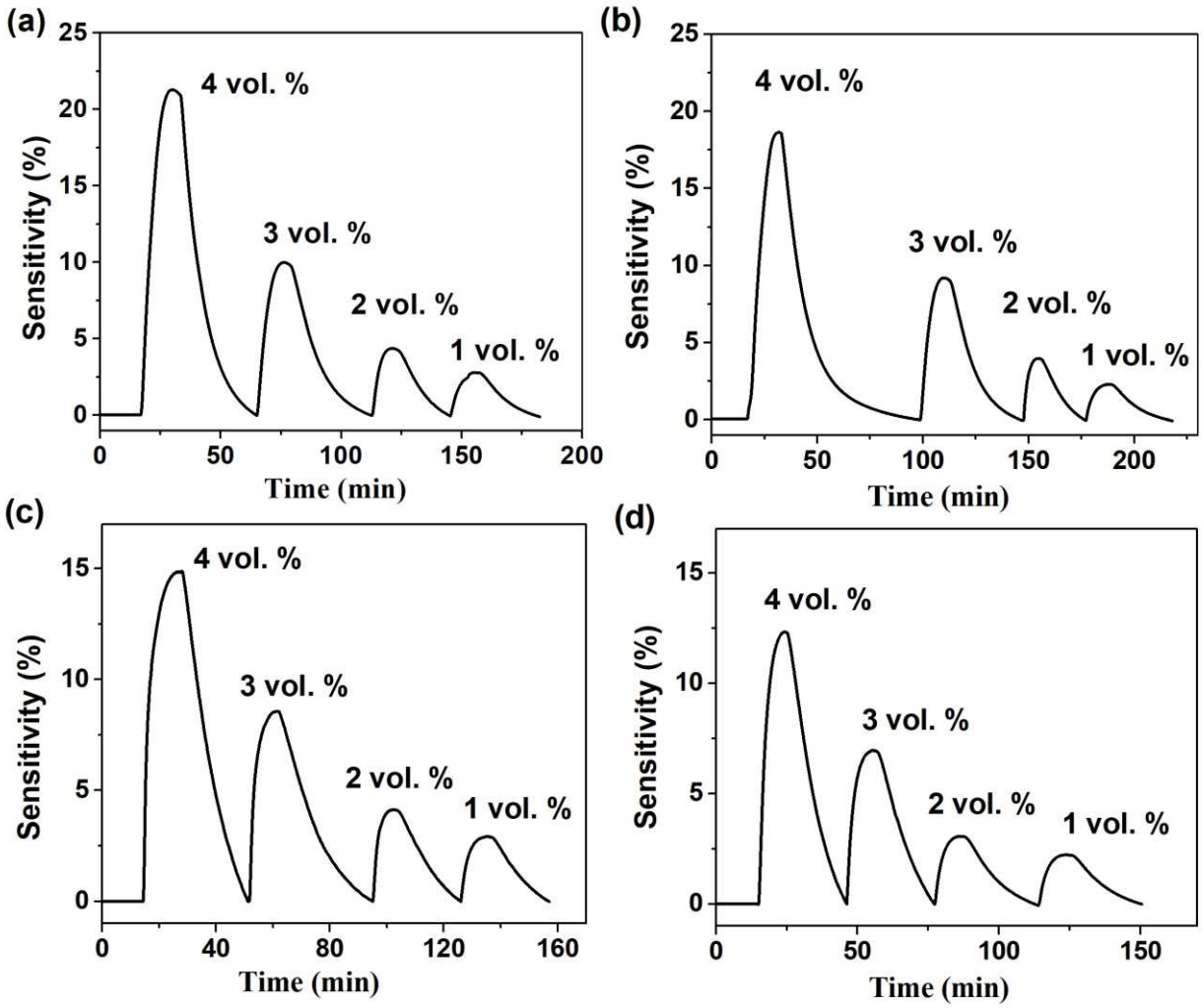



**Figure 7.** Sensitivity versus time at 4, 3, 2 and 1 vol% $H_2$ in air (25 °C) for (a) Pd(33%)/f-graphite on IDE, (b) Pd(33%)/f-graphite on two-fringe, (c) Pd(20%)/f-graphite on IDE and (d) Pd(20%)/f-graphite on two-fringe electrodes.

Figure 8 demonstrates the cyclic repeatability of the same four configurations under repeated on/off exposure to 4 vol% $H_2$. The response and recovery are stable and reproducible over multiple hydrogenation–dehydrogenation cycles, with no progressive drift in peak sensitivity—evidence that the dispersed Pd-on-graphite architecture resists the cracking and agglomeration that degrade continuous Pd films. The peak sensitivities of ≈21%, 19%, 15% and 12% for the four cycles in panels Figure 8a–d for Pd(33%)/f-graphite on IDE, Pd(33%)/f-graphite on two-fringe, Pd(20%)/f-graphite on IDE and Pd(20%)/f-graphite on two-fringe electrodes are registered.

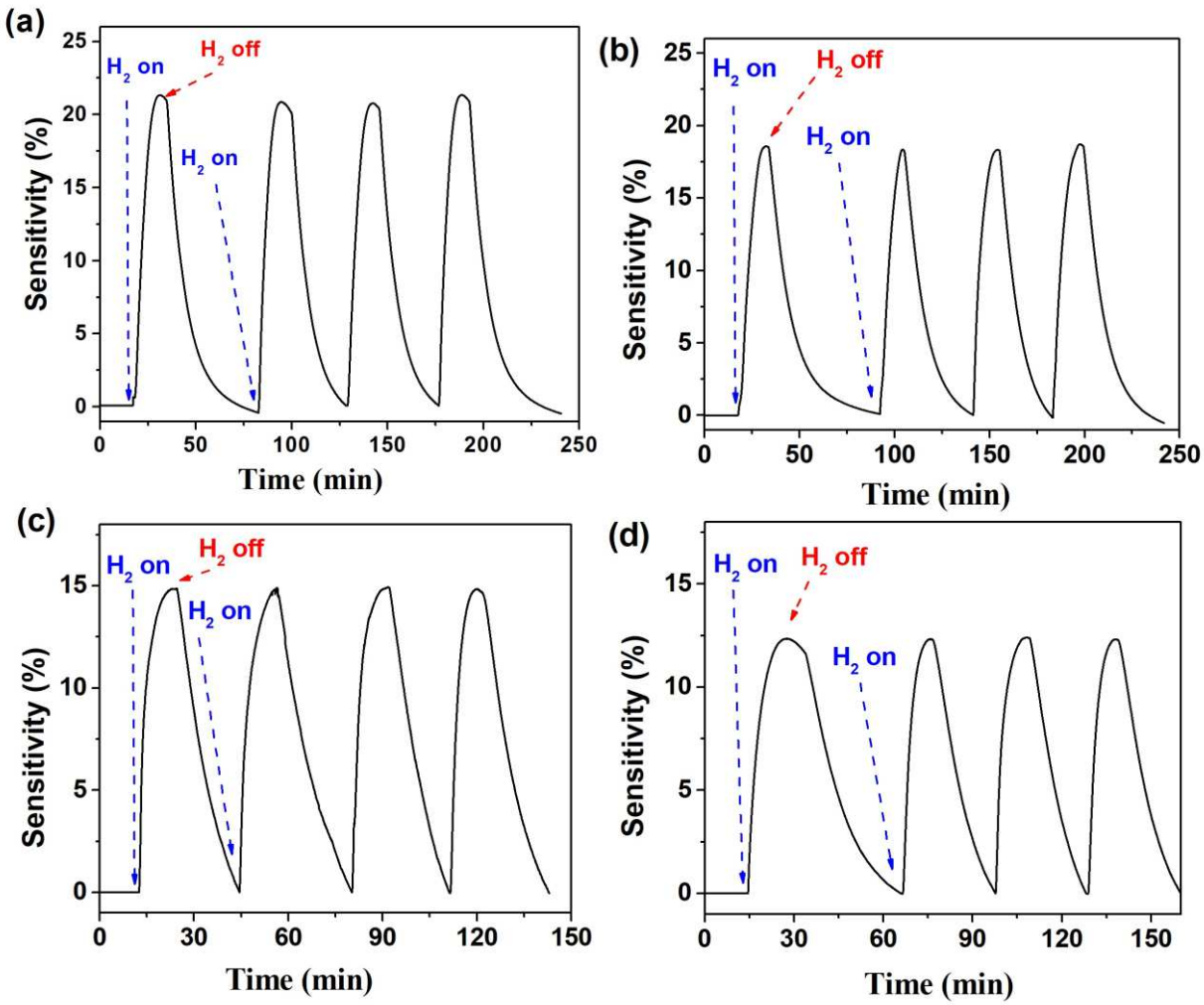



**Figure 8.** Cyclic repeatability of the sensors under repeated 4 vol% $H_2$ on/off exposure for (a) Pd(33%)/f-graphite on IDE, (b) Pd(33%)/f-graphite on two-fringe, (c) Pd(20%)/f-graphite on IDE and (d) Pd(20%)/f-graphite on two-fringe electrodes.

**Table 2.** Sensitivity (at 1–4 vol% $H_2$), IDE = interdigitated electrode; 2-fringe = two-fringe electrode.

| Sample | S @4% | S @3% | S @2% | S @1% |
|---|---|---|---|---|
| Pd(33%)/f-graphite, IDE | 21.3 | 9.9 | 4.3 | 2.7 |
| Pd(33%)/f-graphite, 2-fringe | 18.7 | 9.2 | 3.9 | 2.3 |
| Pd(20%)/f-graphite, IDE | 14.9 | 8.6 | 4.1 | 2.5 |
| Pd(20%)/f-graphite, 2-fringe | 12.3 | 6.9 | 3.1 | 2.2 |

As summarised in Table 2, the best device (33 wt% Pd/f-graphite, IDE) achieves 21.3% sensitivity to 4 vol% H2, with a response time of ≈430 s and a recovery time of ≈1130 s. The response

times are comparable across configurations because they are mainly governed by Pd hydride kinetics, whereas the magnitude of the response is set by Pd loading, dispersion, and electrode geometry. The relatively long recovery reflects the oxygen-mediated water-formation pathway and the diffusion of hydrogen out of the agglomerated Pd. The detailed mechanism is presented in the upcoming section [38].

### 3.6. Hydrogen-sensing mechanism

On exposure to hydrogen, $H_2$ molecules adsorb and dissociate on the Pd nanoparticle surfaces into atomic hydrogen, which is absorbed into the Pd lattice to form a palladium hydride, $PdH_x$:

$$H_2 \rightarrow 2H_{(ads)} \quad \text{and} \quad Pd + xH_{(ads)} \rightarrow PdH_x$$

Hydride formation lowers the work function of Pd relative to both metallic Pd and the carbon support, so electrons are transferred from $PdH_x$ into the f-graphite [15, 39]. Because acid functionalisation renders the graphite weakly p-type (hole-conducting), the injected electrons recombine with holes, reducing the majority-carrier density and thereby increasing the film resistance. The resistance reaches a saturation value set by the equilibrium hydrogen coverage, which is why the response increases with hydrogen concentration. This electron-transfer, work-function-modulation picture is well established for Pd/carbon chemiresistors and is supported by transfer characteristic and Kelvin probe studies in the literature [17, 21, 39].

When the hydrogen supply is removed, recovery is driven by the ambient oxygen: adsorbed atomic hydrogen reacts with $O_2$ to form surface hydroxyls and ultimately water, which desorbs and restores the Pd to its hydrogen-free state, returning the resistance to baseline:

$$4H_{(ads)} + O_2 \rightarrow 2H_2O\uparrow$$

The thin PdO surface layer detected by Raman and inferred from FT-IR participates in this oxygen-mediated step and helps explain why recovery, although complete, is slower than the response. The same charge-transfer logic accounts for the loading dependence: the 33 wt% composite presents more (and better-dispersed) Pd active sites—as shown by FESEM and the stronger Pd XRD reflections—so it transfers more charge per unit hydrogen and yields a larger response than the 20 wt% composite. The interdigitated electrode further increases the response relative to the two-fringe geometry by shortening the conduction path and increasing the sensing area sampled between adjacent fingers.

A quantitative charge-transfer view clarifies why the response is dominated by the Pd/graphite interface rather than by the Pd volume alone. Figure 9a shows the relevant energy-level alignment. Metallic Pd has a work function of ≈5.6 eV, larger than that of the functionalised graphite (≈4.6 eV); hydrogen absorption converts Pd into $PdH_x$, whose work function is lowered to ≈4.5–5.0 eV [27, 40]. The resulting misalignment drives electron transfer from $PdH_x$ into the p-type f-graphite (Figure 9b);

the injected electrons recombine with the majority holes, lowering the carrier concentration and raising the film resistance. The magnitude of the effect, therefore, scales with the density of Pd/graphite junctions—consistent with the loading and dispersion trends from FESEM and XRD—rather than with the total Pd mass, which is the hallmark of interface- (charge-transfer-) controlled sensing.

Two further interfacial processes shape the transient behaviour. First, hydrogen spillover—the migration of Pd-dissociated atomic hydrogen onto the adjacent carbon surface—extends the perturbed region beyond the Pd contact area and increases the effective sensing volume, enhancing sensitivity while contributing to the comparatively slow recovery because spilt-over hydrogen must diffuse back to Pd to be removed. Second, each Pd($PdH_x$)/graphite contact constitutes a nanoscale Schottky-type junction; hydride formation modulates the local band bending and interface barrier, so that conduction through the percolating graphite network is gated by these many parallel nano-junctions. In this percolation-plus-tunnelling picture, the 33 wt% sample, with its denser and better-dispersed Pd population, provides more parallel charge-transfer junctions and hence a larger fractional resistance change than the 20 wt% sample, while the interdigitated electrode geometry samples more of this junction network than the two-fringe layout. This mechanism is fully consistent with, and quantitatively bounded by, the present electrical and spectroscopic data.

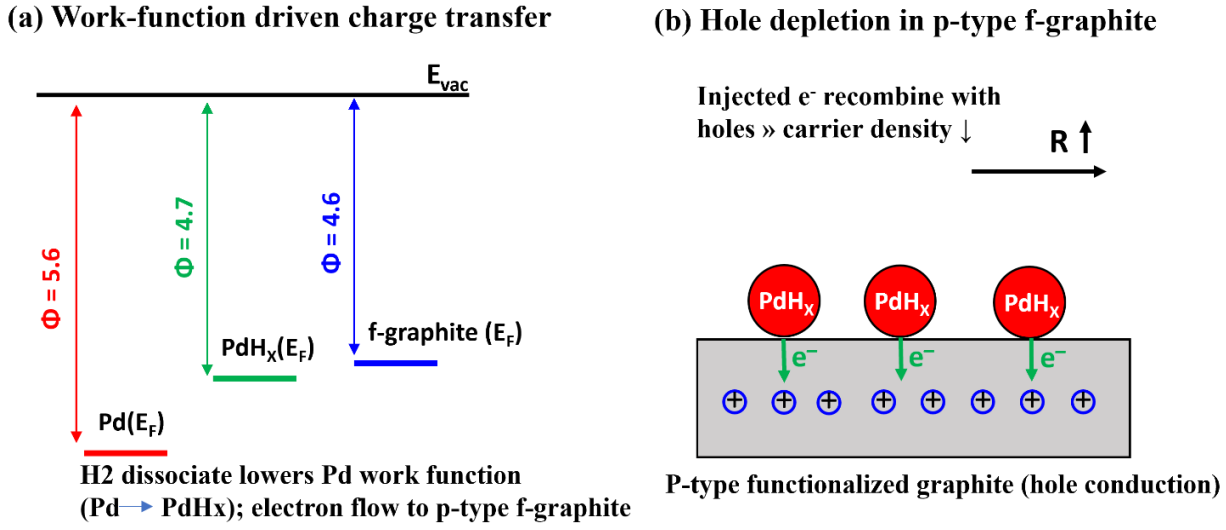



**Figure 9.** Proposed charge-transfer sensing mechanism. (a) Work-function alignment of Pd, $PdH_x$ and p-type f-graphite: hydride formation lowers the Pd work function and drives electron transfer into the graphite. (b) The injected electrons deplete the majority holes of the p-type f-graphite, increasing the film resistance.

To position the present device against the state of the art, Table 3 compares its room-temperature performance with representative carbon-supported and Pd-decorated chemiresistive hydrogen sensors drawn from the literature. Because the definition of "response", the test concentration and the operating conditions differ between studies, the comparison is necessarily indicative rather than a strict ranking; nevertheless, it places the work in context. The present Pd (33 wt%)/f-graphite device delivers a fully-reversible 21.3% response to 4 vol% $H_2$ at 25 °C using an inexpensive bulk-graphite support and a simple, scalable wet-chemical/drop-cast fabrication. Its response magnitude is competitive with, or exceeds, that of the Pt/CNT, Pd/graphene and Pd/rGO chemiresistors listed, while its distinguishing feature is the low-cost graphite support combined with the interface-(charge-transfer-)controlled operation established spectroscopically above. Its main performance gap relative to the fastest nanostructured devices is the recovery time, which the mechanism analysis attributes to spillover-limited desorption and identifies as the primary optimisation target.

Table 3. Comparison of the room-temperature $H_2$-sensing performance of the present Pd/f-graphite device with representative carbon-supported (CNT- and graphene-based) and Pd-decorated chemiresistive hydrogen sensors. Operating conditions and response definitions differ across studies.

| Sensing material | Fabrication/catalyst | $H_2$ conc. | Response (%) | Temp. | Ref. |
|---|---|---|---|---|---|
| Superaligned CNT film | Pt, evaporation | 10 vol% | ~7 | RT | [41] |
| MWCNT | Pt, solution reaction | 4 vol% | 6.5 | RT | [42] |
| MWCNT | Pt, solution reaction | 4 vol% | 8 | RT | [43] |
| Vertically-aligned CNT | Pt, sputtering | 1 vol% | 1.1 | RT | [44] |
| Pt-NPs/SWCNT/graphene nanohybrid | Pt, ALD | 10 vol% | 7.5 | RT | [45] |
| Pd-decorated crumpled rGO | flame aerosol | 2 vol% | 14.8 | RT | [23] |
| Pd NP/graphene | chemical deposition | 1 vol% | 5.88 | RT | [46] |
| Pd-decorated graphene | Pd NP, drop-cast | 0.2 vol% | ~14 ($\Delta G/G$) | RT | [19] |
| Pd nanowires (paper-based) | Pd, solution-grown NWs | 1 vol% | 4.3 | RT | [24] |
| MWCNT@Pd nanosheet | Pd nanosheet composite | 1 vol% | ~0.4 | RT | [47] |
| Pd (33 wt%)/f-graphite, IDE (this work) | wet-chemical + drop-cast | 1 vol% | 21.3 | 25 °C | Present |

## 4. Conclusion

Low-cost chemiresistive hydrogen sensors were fabricated from Pd-decorated functionalised graphite by a simple wet-chemical and drop-casting route. A deliberately cross-correlated characterisation established a single, internally consistent picture of the material: acid functionalisation creates oxygen functionalities and defects (FT-IR, Raman D-band, XRD broadening) that template the growth of 8–12 nm FCC Pd nanoparticles (TEM and XRD Scherrer ≈9 nm) dispersed on the graphite flakes (FESEM), with denser coverage at 33 wt%. Quantitative Raman analysis—I(2D)/I(G) < 1 with a broad, up-shifted 2D band—demonstrates that the support is bulk graphite rather than graphene, correcting a common mis-assignment, while the low-frequency $E_g$ and $B1_g$ bands reveal a thin PdO surface layer. The sensing response is well described by a $PdH_x$-mediated change in work function and by electron transfer to weakly p-type f-graphite, with oxygen-assisted recovery. The best device (33 wt% Pd/f-graphite on an interdigitated electrode) achieved 21.3% sensitivity to 4 vol% $H_2$ at room temperature with full reversibility over repeated cycles, and the sensitivity ordering across loadings and electrode geometries follows directly from the morphological and structural trends. These results show that inexpensive functionalised graphite is a viable alternative to graphene as a Pd support for room-temperature hydrogen sensing, and they identify recovery time as the main avenue for further improvement.

## Acknowledgements

The authors thank their respective institutions for characterisation facilities and support. SR would like to thank the Shenzhen High-Level Talent Program (QY1140900826). B.S acknowledges the Odisha State Higher Education Council, Department of Higher Education, Govt. of Odisha for financial support under MRI funding no. 23EM/PH/123

## Author Contributions (CRediT taxonomy)

P.S.: Conceptualization, Methodology, Investigation, Data curation, Formal analysis, Visualization, Writing – original draft.

B.K.S.: Conceptualization, Methodology, Formal analysis, Visualization, Writing – review & editing, Supervision.

S.R.: Conceptualization, Formal analysis, Visualization, Writing – review & editing, Supervision.

R.N.J.: Formal analysis, Visualization, Writing – review & editing.

All authors reviewed and approved the final manuscript.

## References


[1] S. Mandal, A.V. Marsh, H. Faber, T. Ghoshal, D.K. Goswami, L. Tsetseris, M. Heeney, T.D. Anthopoulos, A robust organic hydrogen sensor for distributed monitoring applications, Nature Electronics, 8 (2025) 343-352.

[2] B. Cui, L. Cheng, X. Xue, J. Jin, L. Huang, Y. Liang, W. Wang, High sensitivity SAW hydrogen gas sensor based on thermal conductivity effect, Microsystems Nanoengineering, 12 (2026) 68.

[3] M. Sangchap, H. Hashtroudi, T. Thathsara, C.J. Harrison, P. Kingshott, A.E. Kandjani, A. Trinchi, M. Shafiei, Exploring the promise of one-dimensional nanostructures: A review of hydrogen gas sensors, International Journal of Hydrogen Energy, 50 (2024) 1443-1457.

[4] T. Hübert, L. Boon-Brett, G. Black, U. Banach, Hydrogen sensors–a review, Sensors Actuators B: Chemical, 157 (2011) 329-352.

[5] P. Sahoo, S.B. Mishra, S. Debata, A. Sharma, B.K. Sahu, S. Padhan, R. Thangavel, B.-K. Lee, Hydrothermally Grown Halogen-Doped ZnO Nanorods for Photoelectrochemical Water Oxidation: Experimental and DFT Insights, The Journal of Physical Chemistry C, 128 (2024) 18711-18723.

[6] P. Sahoo, A. Sharma, S. Padhan, R. Thangavel, Construction of ZnO@ NiO heterostructure photoelectrodes for improved photoelectrochemical performance, International Journal of Hydrogen Energy, 46 (2021) 36176-36188.

[7] L. Boon-Brett, J. Bousek, G. Black, P. Moretto, P. Castello, T. Hübert, U. Banach, Identifying performance gaps in hydrogen safety sensor technology for automotive and stationary applications, International Journal of Hydrogen Energy, 35 (2010) 373-384.

[8] P. Askar, D. Kanzhigitova, A. Ospanova, A. Tapkharov, S. Duisenbekov, M. Abutalip, B. Soltabayev, A. Turlybekuly, S. Adilov, N. Nuraje, 1 ppm-detectable hydrogen gas sensor based on nanostructured polyaniline, Scientific Reports, 14 (2024) 26984.

[9] S. Ghosh, A.B. Roy, D. Nath, S. Bhattacharya, Design and Performance Assessment of ZnO Schottky TFT-based Room Temperature Hydrogen Gas Sensor, Semiconductors, 60 (2026) 88-99.

[10] W.-T. Koo, H.-J. Cho, D.-H. Kim, Y.H. Kim, H. Shin, R.M. Penner, I.-D. Kim, Chemiresistive hydrogen sensors: fundamentals, recent advances, and challenges, ACS nano, 14 (2020) 14284-14322.

[11] C. Prakash, P. Choudhary, A.K. Yadav, M. Sharma, V.K. Singh, A. Dixit, Progress and challenges in nanostructured carbon-based hydrogen sensor, International Journal of Hydrogen Energy, 141 (2025) 896-934.

[12] R. Torkamani, B. Aslibeiki, S. Salari, H. Azizi, D. Peddis, T. Sarkar, High-performance hydrogen gas sensor based on Ag-incorporated ZnO nanoparticles, Scientific Reports, 15 (2025) 38390.

[13] Y.-W. Kuo, R.-J. Wu, U. Fegade, R. Dhake, T. Altalhi, Room temperature hydrogen gas sensor based on α-MnO2/ZnO composite material, Journal of Materials Science: Materials in Electronics, 36 (2025) 1864.

[14] F. Favier, E.C. Walter, M.P. Zach, T. Benter, R.M. Penner, Hydrogen sensors and switches from electrodeposited palladium mesowire arrays, Science, 293 (2001) 2227-2231.

[15] K. Lundström, M. Shivaraman, C. Svensson, A hydrogen-sensitive Pd-gate MOS transistor, Journal of Applied Physics, 46 (1975) 3876-3881.

[16] B. Xie, Y. Liu, Y. Lei, H. Qian, Y. Li, W. Yan, C. Zhou, H.-M. Wen, S. Xia, P. Mao, Innovative Thermocatalytic H2 Sensor with Double-Sided Pd Nanocluster Films on an Ultrathin Mica Substrate, ACS sensors, 9 (2024) 2529-2539.

[17] W. Wu, Z. Liu, L.A. Jauregui, Q. Yu, R. Pillai, H. Cao, J. Bao, Y.P. Chen, S.-S. Pei, Wafer-scale synthesis of graphene by chemical vapor deposition and its application in hydrogen sensing, Sensors Actuators B: Chemical, 150 (2010) 296-300.

[18] M.G. Chung, D.-H. Kim, D.K. Seo, T. Kim, H.U. Im, H.M. Lee, J.-B. Yoo, S.-H. Hong, T.J. Kang, Y.H. Kim, Flexible hydrogen sensors using graphene with palladium nanoparticle decoration, SensorsActuators B: Chemical, 169 (2012) 387-392.

[19] B. Alfano, T. Polichetti, M.L. Miglietta, E. Massera, C. Schiattarella, F. Ricciardella, G. Di Francia, Fully eco-friendly H2 sensing device based on Pd-decorated graphene, Sensors Actuators B: Chemical, 239 (2017) 1144-1152.

[20] D.-T. Phan, G.-S. Chung, A novel Pd nanocube–graphene hybrid for hydrogen detection, Sensors Actuators B: Chemical, 199 (2014) 354-360.

[21] P.A. Pandey, N.R. Wilson, J.A. Covington, Pd-doped reduced graphene oxide sensing films for H2 detection, Sensors Actuators B: Chemical, 183 (2013) 478-487.

[22] B.K. Sahu, G. Kaur, A. Das, Revealing interplay of defects in SnO2 quantum dots for blue luminescence and selective trace ammonia detection at room temperature, ACS applied materials interfaces, 12 (2020) 49227-49236.

[23] M.M. Mohammadi, A. Kumar, J. Liu, Y. Liu, T. Thundat, M.T. Swihart, Hydrogen sensing at room temperature using flame-synthesized palladium-decorated crumpled reduced graphene oxide nanocomposites, ACS sensors, 5 (2020) 2344-2350.

[24] A. Kumar, K. Chen, T. Thundat, M.T. Swihart, Paper based hydrogen sensors using ultrathin palladium nanowires, ACS Applied Materials Interfaces, 15 (2023) 5439-5448.

[25] U. Lange, T. Hirsch, V.M. Mirsky, O.S. Wolfbeis, Hydrogen sensor based on a graphene–palladium nanocomposite, Electrochimica Acta, 56 (2011) 3707-3712.

[26] J. Hong, S. Lee, J. Seo, S. Pyo, J. Kim, T. Lee, A highly sensitive hydrogen sensor with gas selectivity using a PMMA membrane-coated Pd nanoparticle/single-layer graphene hybrid, ACS applied materials interfaces, 7 (2015) 3554-3561.

[27] B.K. Sahu, R.N. Juine, M. Sahoo, R. Kumar, A. Das, Interface of GO with SnO2 quantum dots as an efficient visible-light photocatalyst, Chemosphere, 276 (2021) 130142.

[28] B.K. Sahu, A. Das, Graphene oxide surface chemistry regulated growth of SnO2 nanoparticles for electrochemical application, Journal of Alloys Compounds, 834 (2020) 154901.

[29] K.-H. Kim, M.-S. Jo, S.-H. Kim, B. Kim, J. Kang, J.-B. Yoon, M.-H. Seo, Long-term reliable wireless H2 gas sensor via repeatable thermal refreshing of palladium nanowire, Nature Communications, 15 (2024) 8761.

[30] K. Datta, P. Ghosh, M. More, M. Shirsat, A. Mulchandani, Controlled functionalization of single-walled carbon nanotubes for enhanced ammonia sensing: A comparative study, Journal of Physics D: Applied Physics, 45 (2012) 355305.

[31] R.N. Juine, B.K. Sahu, A. Das, ZnS nano-photocatalysts with elemental type s defects for the visible light harvest and efficient antibiotic, explosive and azo dye pollutants degradation, Journal of Environmental Chemical Engineering, 11 (2023) 111175.

[32] N. Colthup, Introduction to infrared and Raman spectroscopy, Elsevier2012.

[33] A.C. Ferrari, J.C. Meyer, V. Scardaci, C. Casiraghi, M. Lazzeri, F. Mauri, S. Piscanec, D. Jiang, K.S. Novoselov, S. Roth, Raman spectrum of graphene and graphene layers, Physical review letters, 97 (2006) 187401.

[34] A.C. Ferrari, Raman spectroscopy of graphene and graphite: Disorder, electron–phonon coupling, doping and nonadiabatic effects, Solid state communications, 143 (2007) 47-57.

[35] A.C. Ferrari, D.M. Basko, Raman spectroscopy as a versatile tool for studying the properties of graphene, Nature nanotechnology, 8 (2013) 235-246.

[36] K.N. Kudin, B. Ozbas, H.C. Schniepp, R.K. Prud'Homme, I.A. Aksay, R. Car, Raman spectra of graphite oxide and functionalized graphene sheets, Nano letters, 8 (2008) 36-41.

[37] J. McBride, K. Hass, W. Weber, Resonance-Raman and lattice-dynamics studies of single-crystal PdO, Physical Review B, 44 (1991) 5016.

[38] R. Duś, R. Nowakowski, E. Nowicka, Chemical and structural components of work function changes in the process of palladium hydride formation within thin Pd film, Journal of alloys compounds, 404 (2005) 284-287.

[39] F. Schedin, A.K. Geim, S.V. Morozov, E.W. Hill, P. Blake, M.I. Katsnelson, K.S. Novoselov, Detection of individual gas molecules adsorbed on graphene, Nature materials, 6 (2007) 652-655.

[40] J. Kong, N.R. Franklin, C. Zhou, M.G. Chapline, S. Peng, K. Cho, H. Dai, Nanotube molecular wires as chemical sensors, Science, 287 (2000) 622-625.

[41] D. Jung, M. Han, G.S. Lee, Fast-response room temperature hydrogen gas sensors using platinum-coated spin-capable carbon nanotubes, ACS applied materials interfaces, 7 (2015) 3050-3057.

[42] M.K. Kumar, S. Ramaprabhu, Nanostructured Pt functionlized multiwalled carbon nanotube based hydrogen sensor, The Journal of Physical Chemistry B, 110 (2006) 11291-11298.

[43] A. Kaniyoor, S. Ramaprabhu, Hybrid carbon nanostructured ensembles as chemiresistive hydrogen gas sensors, Carbon, 49 (2011) 227-236.

[44] M. Penza, R. Rossi, M. Alvisi, M. Signore, G. Cassano, D. Dimaio, R. Pentassuglia, E. Piscopiello, E. Serra, M. Falconieri, Characterization of metal-modified and vertically-aligned carbon nanotube films for functionally enhanced gas sensor applications, Thin Solid Films, 517 (2009) 6211-6216.

[45] B. Liu, M. Alamri, M. Walsh, J.L. Doolin, C.L. Berrie, J.Z. Wu, interfaces, Development of an ALD-Pt@ SWCNT/graphene 3D nanohybrid architecture for hydrogen sensing, ACS applied materials, 12 (2020) 53115-53124.

[46] X. Tang, P.-A. Haddad, N. Mager, X. Geng, N. Reckinger, S. Hermans, M. Debliquy, J.-P. Raskin, Chemically deposited palladium nanoparticles on graphene for hydrogen sensor applications, Scientific reports, 9 (2019) 3653.

[47] A. Kumar, Y. Zhao, M.M. Mohammadi, J. Liu, T. Thundat, M.T. Swihart, Palladium nanosheet-based dual gas sensors for sensitive room-temperature hydrogen and carbon monoxide detection, ACS sensors, 7 (2022) 225-234.